Electrodipping Force Acting on Solid Particles at a Fluid Interface

Krassimir D. Danov, Peter A. Kralchevsky,* and Mariana P. Boneva

Laboratory of Chemical Physics & Engineering, Faculty of Chemistry, University of Sofia, 1 James Bourchier Avenue, 1164 Sofia, Bulgaria

Received February 3, 2004. In Final Form: April 30, 2004

We report experimental results which show that the interfacial deformation around glass particles (radius, 200−300 μm) at an oil−water (or air−water) interface is dominated by an electric force, rather than by gravity. It turns out that this force, called for brevity "electrodipping," is independent of the electrolyte concentration in the water phase. The force is greater for oil−water than for air−water interfaces. Under our experimental conditions, it is due to charges at the particle−oil (instead of particle−water) boundary. The derived theoretical expressions, and the experiment, indicate that this electric force pushes the particles into water. To compute exactly the electric stresses, we solved numerically the electrostatic boundary problem, which reduces to a set of differential equations. Convenient analytical expressions are also derived. Both the experimental and the calculated meniscus profile, which are in excellent agreement, exhibit a logarithmic dependence at long distances. This gives rise to a long-range electric-field-induced capillary attraction between the particles, detected by other authors. Deviation from the logarithmic dependence is observed at short distances from the particle surface due to the electric pressure difference across the meniscus. The latter effect gives rise to an additional short-range contribution to the capillary interaction between two floating particles. The above conclusions are valid for either planar or spherical fluid interfaces, including emulsion drops. The electrodipping force, and the related long-range capillary attraction, can engender two-dimensional aggregation and self-assembly of colloidal particles. These effects could have implications for colloid science and the development of new materials.

1. Introduction

The weight of a particle attached to a fluid surface creates interfacial deformation (Figure 1). If the distortions around two such particles overlap, the latter experience a strong capillary attraction that forces them to aggregate.[1,2] Interfacial deformations appear also when particles are captured in a liquid film of a thickness smaller than their diameter. The resulting capillary forces[3] have been found to cause self-assembly and aggregation of particles of various sizes, including viruses and protein macromolecules.[4−7] In general, the magnitude of the interfacial deformation, characterized by the slope angle, ψ, is determined from the condition $2\pi r_c\gamma \sin\psi = F$; that is, the surface tension force exactly counterbalances the applied normal external force, F; γ is the interfacial tension (see Figure 1 for the other notation).

If the normal force is due to gravity, then $F \propto R^3$ (R = particle radius), and the magnitude of the surface distortion decreases fast with the diminishment of particle size. Typically, for $R < 10\,\mu$m, the deformation is so small that the energy of the gravity-driven capillary attraction becomes negligible.[4,6,7] However, as suggested by Nikolaides et al.,[8] for such small particles (including nanoparticles), the normal force, F, could be of electric (rather than gravitational) origin, and then, interfacial distortions and lateral capillary forces will appear, as in the case of bigger heavy particles.

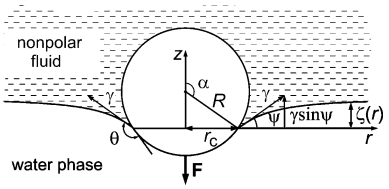

Figure 1. Sketch of a particle at the interface between water and a nonpolar fluid (oil, air, etc.). γ is the interfacial tension; R and r_c are the radii of the particle and the three-phase contact line; α and θ are the central and contact angle; ψ is the meniscus slope angle at the contact line; **F** is a normal force acting on the particle, which can be of electric or gravitational origin (weight and buoyancy); and $z = \zeta(r)$ describes the meniscus profile.

Long-range attractive forces between micrometer-sized particles at a fluid interface were experimentally detected[8−12] and attributed[8] to capillary interaction, which originates from interfacial distortions created by the particle electric field. The latter explanation was called into question[13] on the argument that the pressure difference, produced by the electric stresses, engenders a distortion and

* To whom correspondence should be addressed. Current address: LCPE, Faculty of Chemistry, Sofia University, 1 James Bourchier Ave., 1164 Sofia, Bulgaria. Phone: (+359) 2-962 5310. Fax: (+359) 2-962 5643. E-mail: pk@lcpe.uni-sofia.bg.

(1) Nicolson, M. M. *Proc. Cambridge Philos. Soc.* **1949**, *45*, 288.
(2) Chan, D. Y. C.; Henry, J. D.; White, L. R. *J. Colloid Interface Sci.* **1981**, *79*, 410.
(3) Kralchevsky, P. A.; Paunov, V. N.; Ivanov, I. B.; Nagayama, K. *J. Colloid Interface Sci.* **1992**, *151*, 79.
(4) Denkov, N. D.; Velev, O. D.; Kralchevsky, P. A.; Ivanov, I. B.; Yoshimura, H.; Nagayama, K. *Langmuir* **1992**, *8*, 3183.
(5) Yamaki, M.; Higo, J.; Nagayama, K. *Langmuir* **1995**, *11*, 2975.
(6) Kralchevsky, P. A.; Nagayama, K. *Particles at Fluid Interfaces and Membranes*; Elsevier: Amsterdam, The Netherlands, 2001.
(7) Kralchevsky, P. A.; Denkov, N. D. *Curr. Opin. Colloid Interface Sci.* **2001**, *6*, 383.
(8) Nikolaides, M. G.; Bausch, A. R.; Hsu, M. F.; Dinsmore, A. D.; Brenner, M. P.; Gay, C.; Weitz, D. A. *Nature* **2002**, *420*, 299.
(9) Ghezzi, F.; Earnshaw, J. C. *J. Phys.: Condens. Matter* **1997**, *9*, L517.
(10) Ruiz-Garcia, J.; Gámez-Corrales, R.; Ivlev, B. I. *Physica A* **1997**, *236*, 97.
(11) Ruiz-Garcia, J.; Gámez-Corrales, R.; Ivlev, B. I. *Phys. Rev. E* **1998**, *58*, 660.
(12) Stamou, D.; Duschl, C.; Johannsmann, D. *Phys. Rev. E* **2000**, *62*, 5263.
(13) Megens, M.; Aizenberg, J. *Nature* **2003**, *424*, 1014.

10.1021/la0497090 CCC: $27.50
Published on Web 06/16/2004

capillary force of much shorter range than necessary to explain the data reported in ref 8.

Our purpose here is to verify experimentally whether the electric field around a charged particle at a fluid interface can really cause a significant interfacial deformation and to investigate whether the latter deformation is sufficiently long-ranged to cause the experimentally detected attractive force.[8] We established that the electric-field-induced deformation could be observed with larger particles, say $R \approx 200-300\ \mu$m, for which the meniscus profile can be directly investigated by optical microscope.

The paper is organized as follows. In section 2, we describe the experiment and present data for the deformation caused by glass spheres at oil−water and air−water interfaces. Next, we discuss the experimental data, the theoretical predictions about the meniscus shape, and the related lateral capillary force between two particles. In the subsequent three sections, we develop theoretical approaches which allow one to calculate the electric forces acting on the three interfaces in the considered system: particle−water, particle−oil, and water−oil. The results are valid for any dielectric solid particle (not necessarily glass) and for any nonpolar fluid (not necessarily oil).

The obtained experimental results provide direct proof for the existence of strong normal electric forces experienced by charged solid particles at the water−nonpolar fluid boundary. Our data and theoretical analysis indicate that a long-range (logarithmic) meniscus deformation always exists (in addition to the short-range electric deformation) and engenders the long-range attractive capillary force, which gives explanation to the experimental findings in ref 8. We observed also short-range meniscus deformations due to an electrically induced pressure difference, which had been previously discussed.[8,13] These results could have important implications for colloid science, including particle-stabilized Pickering emulsions[14] and development of new materials.[15−20]

2. Experiments and Data Analysis

2.1. Experimental System and Results. In our experiments, the water phase was pure deionized water or an aqueous NaCl solution of concentration C. The oil phase was tetradecane, which has a density of $\rho_n = 0.763$ g/cm^3, a dielectric constant of $\epsilon_n = 2.04$, and an interfacial tension against water of $\gamma = 52.2$ mN/m. The experiments were carried out at 23 °C.

As solid particles, we used silanized glass spheres of density $\rho_p = 2.62$ g/cm^3 and dielectric constant $\epsilon_p = 3.97$; see Tables 1 and 2 for data about the sphere radius, R, and the contact angle, θ, at the tetradecane−water and air−water interfaces (Figure 1).

Before the silanization, the glass particles were kept for 2 h in sulfochromic acid to clean their surfaces. After that, the acid was poured out and the particles were rinsed abundantly by pure deionized water. Next, the particles were kept for 6 h in a 0.01 M solution of NaOH, and subsequently, they were rinsed again by deionized water. Further, the particles were dried for 10 h at 80 °C. Next, we dropped ∼40 μL of hexamethyldisilazane (HMDS) in the Petri dish, which contained the particles. The dish was kept for 1 h in a vacuum dryer until the complete evaporation of HMDS occurred. After this silanization procedure, the glass spheres were stored in pure ethanol. Before each experiment, the sphere was first dried at room temperature and then placed at the fluid interface.

The experimental cell is a rectangular glass box of sides from optical plane-parallel plates. The height of the cell is 55 mm. The horizontal cross section of the cell has dimensions of 80 × 25 mm^2, both of them being markedly greater than the characteristic capillary length, $(\Delta\rho g/\gamma)^{-1/2}$; the latter is 4.7 and 2.7 mm, respectively, for the tetradecane−water and air−water interfaces; $\Delta\rho$ is the difference between the mass densities of the two fluid phases and g is the acceleration due to gravity. The inner walls of the cell are moderately hydrophobized (contact angle, ≈80° across water). Thus, a slightly concave tetradecane−water or air−water meniscus is formed, which decays exponentially at a

Table 1. Tetradecane−Water Interface: Data for Glass Spheres of Radius R at Various NaCl Concentrations, C

C (M)	r_c (μm)	θ (deg)	ψ (deg)	$\psi^{(g)}$ (deg)	$F^{(g)}$ (μN)	$F^{(el)}$ (μN)	σ_{pn} (μC/m^2)
			$R = 240.61\ \mu$m				
0.0000	235.13	115.21	12.97	0.7548	1.0159	16.023	70.89
0.0033	236.29	112.95	12.09	0.7494	1.0136	15.673	70.19
0.0099	236.32	112.93	12.11	0.7492	1.0135	15.562	70.31
0.0164	235.72	114.08	12.52	0.7521	1.0148	15.686	70.50
0.0259	236.18	113.79	12.79	0.7499	1.0138	16.076	71.09
0.0415	236.76	113.05	12.80	0.7471	1.0126	16.022	71.24
0.0566	236.56	113.12	12.61	0.7481	1.0130	15.858	70.87
0.0627	236.98	112.23	12.28	0.7461	1.0121	15.672	71.12
			$R = 210.23\ \mu$m				
0.0867	198.82	121.36	12.42	0.6014	0.6845	13.296	69.19
0.1216	200.21	120.59	12.86	0.5962	0.6833	13.886	69.55
0.1552	200.37	120.35	12.76	0.5956	0.6831	13.787	69.41
			$R = 231.02\ \mu$m				
0.0000	220.65	120.46	13.24	0.7174	0.9062	15.616	69.58
0.0033[a]	226.00	114.88	12.90	0.6946	0.8986	15.590	70.91
			$R = 263.24\ \mu$m				
0.0000	253.20	122.53	16.68	0.9230	1.3377	22.395	71.16
0.0033	252.90	122.77	16.69	0.9244	1.3382	22.372	70.90
			$R = 214.44\ \mu$m				
0.0000	200.00	126.04	14.89	0.6368	0.7291	16.077	70.97
0.0066	206.10	119.11	12.98	0.6137	0.7237	14.405	70.78
0.0456	203.20	122.34	13.54	0.6253	0.7266	14.814	69.62
			$R = 210.61\ \mu$m				
0.9677	205.14	114.33	11.24	0.5811	0.6823	12.392	69.80
1.0000	204.16	115.84	11.62	0.5849	0.6836	12.763	69.63
			$R = 200.59\ \mu$m				
0.9677	183.25	128.55	14.55	0.5711	0.5990	14.462	70.49
1.0000	179.35	131.89	15.28	0.5854	0.6010	14.863	70.52

[a] This row of the table corresponds to the photo in Figure 2.

Table 2. Air−Water Interface: Data for Glass Spheres of Radius R at Various NaCl Concentrations, C

C (M)	r_c (μm)	θ (deg)	ψ (deg)	$\psi^{(g)}$ (deg)	$F^{(g)}$ (μN)	$F^{(el)}$ (μN)	σ_{pn} (μC/m^2)
			$R = 232.52\ \mu$m				
0.0000	207.73	119.08	2.385	0.7643	1.2570	2.6337	25.60
0.0019	208.63	118.72	2.521	0.7595	1.2546	2.8754	26.80
0.0038	207.45	119.26	2.404	0.7658	1.2577	2.6587	25.70
0.0083	207.00	119.68	2.584	0.7681	1.2589	2.9416	27.01
0.0120	205.04	120.63	2.497	0.7785	1.2638	2.7574	26.06
0.0170	205.64	120.15	2.329	0.7753	1.2623	2.4993	24.83
			$R = 228.05\ \mu$m				
1.0000	204.25	118.77	2.365	0.7325	1.1846	2.6097	26.01
			$R = 294.23\ \mu$m				
1.0000	271.23	115.73	2.921	1.1675	2.5070	3.6873	24.46
			$R = 288.79\ \mu$m				
1.0000	272.20	112.26	2.741	1.0839	2.3360	3.4973	24.94
			$R = 272.52\ \mu$m				
1.0000	253.65	114.20	2.749	0.9861	1.9802	3.4785	25.91

(14) Aveyard, R.; Binks, B. P.; Clint, J. H. *Adv. Colloid Interface Sci.* **2003**, *100−102*, 503.
(15) Velev, O. D.; Furusawa, K.; Nagayama, K. *Langmuir* **1996**, *12*, 2374.
(16) Burmeister, F.; Schäfle, C.; Keilhofer, B.; Bechinger, C.; Boneberg, J.; Leiderer, P. *Adv. Mater.* **1998**, *10*, 495.
(17) Qin, D.; Xia, Y.; Xu, B.; Yang, H.; Zhu, C.; Whitesides, G. M. *Adv. Mater.* **1999**, *11*, 1433.
(18) Bowden, N.; Arias, F.; Deng, T.; Whitesides, G. M. *Langmuir* **2001**, *17*, 1757.
(19) Dinsmore, A. D.; Hsu, M. F.; Nikolaides, M. G.; Marquez, M.; Bausch, A. R.; Weitz, D. A. *Science* **2002**, *298*, 1006.
(20) Truskett, V. N.; Stebe, K. J. *Langmuir* **2003,** *19*, 8271.

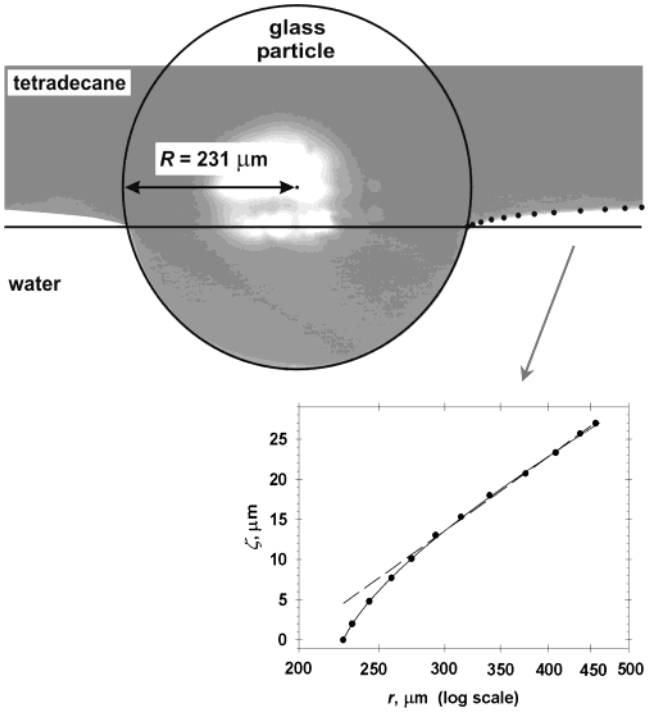

Figure 2. Side-view photo of a spherical glass particle at the water−tetradecane interface. From the photo, we measure $\psi = 12.9°$. If the interfacial deformation were produced by the gravity force alone, ψ would be only 0.75°. The difference can be attributed to the electrodipping force. Coordinates of points from the meniscus profile, $z = \zeta(r)$, are digitized and plotted vs log(r) in the inset. Close to the contact line, the plot ζ vs log(r) deviates from the straight line; this is a result of the action of electric stresses. The continuous curve in the inset, which excellently agrees with the data points, is the meniscus profile computed by numerical solution of the electrostatic boundary problem with no adjustable parameters (details in the text).

relatively short distance from the walls. Thus, the meniscus around the central part of the cell is horizontal.

Before the experiments, the glass cell was subjected to the following cleaning procedure. First, the cell was rinsed by ethanol. Then, it was kept for 5 min in boiling deionized water. After cooling, the cell was filled with a 1:1:5 mixture of 25% NH_3 + 30% H_2O_2 + H_2O and heated in a water bath for 25 min at 60−80 °C. The same procedure was then repeated but with 25% HCl solution instead of the 25% NH_3 solution. Finally, the cell was rinsed again with deionized water and dried for 2 h at 30 °C.

The observations were carried out by means of a horizontal microscope, equipped with a long-focus objective and connected to a monitor and video-recording system. In the absence of the particle, a horizontal interface was seen. After inserting the particle, we observed deformations of the interface (deviations from planarity), as in the photo in Figure 2.

By computer image analysis of the video frames, like that in Figure 2, we measured directly the particle radius, R, the contact-line radius, r_c, and the meniscus slope angle at the contact line, ψ (see the data in Tables 1 and 2). The value of each parameter is an average of at least 10 measurements. The measurements were accurate and reproducible; the standard error of mean was typically on the order of 0.1% for R and r_c, while the absolute error of the angle ψ was not greater than 0.2°. From the measured parameters, we calculated the contact angle: $\theta = \psi + \alpha$, where α is a central angle and $\alpha = \arcsin(r_c/R)$; see Figure 1. (As the arcsine is a two-valued function, one should keep in mind whether the angle α is acute or obtuse.)

In some experiments, after the particle was placed at the interface, by micropipet we added small consecutive portions of concentrated NaCl solution to increase the ionic strength, C, of the aqueous phase. The purpose was to check whether C influences the angle ψ. The addition of NaCl slightly disturbs the interface, which leads to some small scattering of the values of r_c, ψ, and θ, obtained for the same particle (the same R) at different steps of this procedure (at different C); see Tables 1 and 2. This data scattering can be attributed to a small contact angle hysteresis, rather than to a systematic effect of C.

Tables 1 and 2 show the obtained results for a number of glass spheres (identified by their radius, R) at the tetradecane−water and air−water boundaries. The information in each row is extracted from a photo, like that in Figure 2. From the measured R, r_c, and ψ values, we further calculate other parameters of the system, such as the gravitational and electric forces acting on the particle, $F^{(g)}$ and $F^{(el)}$, the surface electric charge density, σ_{pn}, at the particle−nonpolar fluid (oil, air, etc.) boundary, etc.; the obtained values are also given in Tables 1 and 2. The next subsection explains how the latter parameters have been determined.

2.2. Parameters Calculated from the Experimental Data. The gravity force, $F^{(g)}$, is equal to the difference between the particle weight and the buoyancy (Archimedes) force. For a sphere at a fluid interface, we have (see, e.g., eq 32 in ref 21)

$$F^{(g)} = g[(\rho_p - \rho_w)V_w + (\rho_p - \rho_n)V_n - (\rho_w - \rho_n)\pi r_c^2 h_c] \quad (2.1)$$

where, as usual, ρ_p, ρ_w, and ρ_n are the mass densities of the particle, water, and nonpolar fluid (oil, air, etc.); V_w and V_n are the portions of the particle volume immersed, respectively, in water and in the nonpolar fluid; and h_c is the vertical distance between the plane of the contact line and the plane of the horizontal fluid interface far from the particle. Geometrical considerations give

$$V_n = (^4/_3)\pi R^3 - V_w$$
$$V_w = (^1/_3)\pi R^3(2 + 3\cos\alpha - \cos^3\alpha) \quad (2.2)$$

Although the term with h_c in eq 2.1 is usually negligible, it was taken into account in our computations, where the Derjaguin formula[22] was used:

$$h_c = -r_c \sin\psi \ln[qr_c\gamma_e(1 + \cos\psi)/4] \quad q = (\Delta\rho g/\gamma)^{1/2} \quad (2.3)$$

Here, $\Delta\rho = \rho_w - \rho_n$; $\gamma_e = 1.781\,072\,418...$ is the Euler−Masceroni constant. The Derjaguin formula is valid for $(qr_c)^2 \ll 1$, which is fulfilled for our particles (200 μm < R < 300 μm). From the calculated $F^{(g)}$ value, we can determine how large the meniscus slope angle would be at the contact line if only $F^{(g)}$ were acting on the particle:

$$\sin\psi^{(g)} = F^{(g)}/(2\pi\gamma r_c) \quad (2.4)$$

In Tables 1 and 2, the values of $\psi^{(g)}$, calculated from the latter equation, are compared with the experimental angle ψ, measured directly from the photos. For the tetradecane−water interface (Table 1), the experimental ψ angle is much greater than the calculated $\psi^{(g)}$ angle. This is the biggest and most important effect reported in the present study, which indicates that the gravitational force, alone, cannot explain the observed deformation of the fluid interface around the particle. The same effect, although of smaller magnitude, is observed for the air−water interface (Table 2); the difference between ψ and $\psi^{(g)}$ is smaller but systematic.

It is natural to hypothesize that the difference between ψ and $\psi^{(g)}$ is due to an electric force, $F^{(el)}$, that pushes the particles into water. $F^{(el)}$ can be calculated from the balance of forces exerted on the particle:

$$F^{(el)} = 2\pi r_c\gamma \sin\psi - F^{(g)} \quad (2.5)$$

The values of $F^{(el)}$, calculated from eq 2.5, are given in Tables 1 and 2. It is interesting to note, that the obtained values of $F^{(el)}$ are insensitive to the NaCl concentration in water, C. To illustrate this, in Figure 3, we have plotted the data for the first particle in Table 1 (with $R = 240.6\,\mu$m). In the same figure, we compare

(21) Ivanov, I. B.; Kralchevsky, P. A.; Nikolov, A. D. *J. Colloid Interface Sci.* **1986**, *112*, 97.

(22) Derjaguin, B. V. *Dokl. Akad. Nauk SSSR* **1946**, *51*, 517.

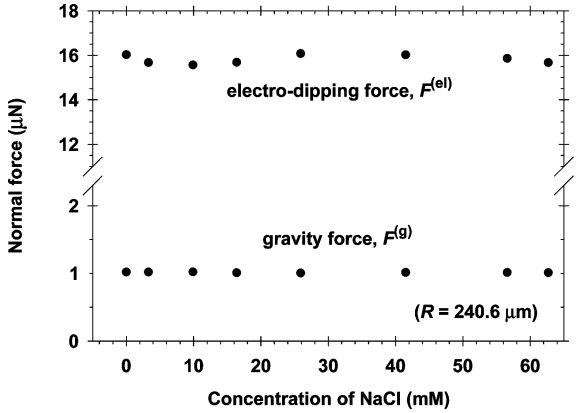

Figure 3. Plot of the normal force vs the NaCl concentration, C, which is varied by adding consecutive portions of NaCl into water: results for a single glass particle at the tetradecane−water interface. R, r_c, and ψ are measured from photos, like in Figure 2. Then, $F^{(g)}$ and $F^{(el)}$ are calculated from eqs 2.1 and 2.5. One sees that $F^{(el)} \gg F^{(g)}$ and that $F^{(el)}$ is independent of C.

the values of $F^{(el)}$ and $F^{(g)}$ for this particle. The independence of $F^{(el)}$ from C indicates that $F^{(el)}$ is caused by charges, of density σ_{pn}, at the oil−water (or air−water) interface. The existence of such surface charges has been identified as the reason for the observed strong lateral repulsion between colloidal particles at an oil−water interface.[23,24] We proved our hypothesis, that the found difference between ψ and $\psi^{(g)}$ is due to an electric force engendered by σ_{pn}, in the following way. From the values of $F^{(el)}$ (Tables 1 and 2), we first calculated σ_{pn}; see the last columns of Tables 1 and 2. Then, using the determined σ_{pn} value, we computed the electric pressure, p_{el}, exerted at the oil−water interface in the vicinity of the particle. Further, taking into account the effect of p_{el}, we solved the Laplace equation of capillarity and determined the meniscus shape around the particle, $z = \zeta(r)$, which is seen in the experimental video frames. The computed $\zeta(r)$ curve compares excellently with the experimental points; see the inset in Figure 2; there are *no adjustable parameters*. In particular, the meniscus deviates from the $\ln(r)$ dependence close to the particle surface (inset of Figure 2) due to the effect of p_{el} (details in sections 3.5 and 6.1 below). This perfect agreement between theory and experiment proves our hypothesis about the existence of $F^{(el)}$ and its origin. The realization of this program demanded considerable theoretical work, which is described in the rest of this paper.

Before continuing with the theory, let us note that the values of σ_{pn}, calculated from $F^{(el)}$ (Tables 1 and 2), are practically the same for all investigated particles and NaCl concentrations. The average values are $\sigma_{pn} = 25.7 \pm 0.8\ \mu C/m^2$ for the glass−air interface and $\sigma_{pn} = 70.4 \pm 0.7\ \mu C/m^2$ for the glass−tetradecane interface. The latter value is close to the value $\sigma_{pn} \approx 80\ \mu C/m^2$ reported[24] for the silanized silica−hydrocarbon boundary.

Our experiments showed that the effect of $F^{(el)}$ is present not only for tetradecane but also for other liquid hydrocarbons, including dodecane, xylene, and triglycerides.

3. Theoretical Background

3.1. Electric Force at the Particle−Water Interface. Let us consider a charged spherical particle in the bulk of an aqueous solution. At equilibrium, the tangential and normal components of the pressure tensor (with respect to the surface of the colloidal sphere), P_T and P_N, obey the relationship[25]

$$\frac{dP_N}{dr} = \frac{2}{r}(P_T(r) - P_N(r)) \qquad (3.1)$$

where r is the radial coordinate. Substituting in eq 3.1 available expressions for P_T and P_N for an electric double layer,[6,26] one can check that $dP_N/dr > 0$ (details in section 4). In other words, the normal pressure close to the particle surface, $P_N(R)$, is lower than the bulk pressure, $P_N(\infty)$. In the case of a particle at an oil−water interface (Figure 1), the derived pressure difference, $\Delta P_N = P_N(\infty) - P_N(R)$, is exerted on the portion of the particle surface which is immersed in water. This leads to a normal force, $F^{(w)} = \pi r_c^2 \Delta P_N$, which pulls the particle into the aqueous phase. When the thickness of the electric double layer, κ^{-1}, is much smaller than the particle radius ($\kappa R \gg 1$), we derive (section 4)

$$F^{(w)} = \pi r_c^{\,2} \frac{p}{\kappa R} \qquad (3.2)$$

$$p \equiv 16CkT\{[(\kappa\sigma_{pw})^2/(4eC)^2 + 1]^{1/2} - 1\} \qquad (3.3)$$

where p is independent of R, k is the Boltzmann constant, T is the temperature, κ is the Debye screening parameter and $\kappa^2 = (2e^2C/\epsilon_0\epsilon_w kT)$, e is the elementary charge, ϵ_0 is the dielectric permittivity of vacuum, ϵ_w is the dielectric constant of water, and σ_{pw} is the electric charge density at the particle−water boundary.

To estimate $F^{(w)}$ for the particle in Figure 3 ($R = 240.6\ \mu m$, $r_c = 236\ \mu m$), let us take a typical experimental value, $\sigma_{pw} = 1780\ \mu C/m^2$ (90 nm^2 per surface charge), at the glass−water interface ($C = 0.1$ mM, pH = 5.8).[27] From eqs 3.2 and 3.3, we estimate $F^{(w)} = 0.07\ \mu N$, which is much smaller than the values of $F^{(el)}$ in Tables 1 and 2 and in Figure 3, in agreement with the conclusion that in our case $F^{(el)}$ is dominated by the electric force exerted at the particle−oil (rather than particle−water) interface. On the other hand, for the smaller particles in the experiments by Nikolaides et al.,[8] $F^{(w)}$ certainly has an essential effect in view of the influence of electrolyte concentration on the particle ordering established in ref 8; see section 3.7 below.

3.2. Electric Force at the Particle−Nonpolar Fluid Interface. Electric charges present at the particle−nonpolar fluid (oil, air, etc.) boundary give rise to an additional contribution to the normal force (details in section 5):

$$F^{(n)} = \frac{\sigma_{pn}^2 R^2}{\epsilon_0 \epsilon_n}(1 - \cos\alpha)\, f(\alpha, \epsilon_p/\epsilon_n) \qquad (3.4)$$

$F^{(n)}$ (just like $F^{(w)}$) pushes the particles into water; as before, $\sin\alpha = r_c/R$ and σ_{pn} is the electric charge density at the particle−nonpolar phase boundary; ϵ_p and ϵ_n are the dielectric constants of the particle and nonpolar fluid; and f is a universal dimensionless function of the ratio ϵ_p/ϵ_n and the angle α. The bulk charge density in the nonpolar fluid is zero; therefore, the electrostatic interactions therein are long-ranged and $F^{(n)}$ is sensitive to the geometry of the system, accounted for by the dependence on the angle α (eq 3.4). We computed f (see Figure 4) by solving numerically the respective electrostatic boundary problem. In the Appendix, we present a convenient way to obtain numerical values of the function $f(\alpha, \epsilon_p/\epsilon_n)$ by polynomial interpolation. Note that eq 3.4 gives the leading term in $F^{(n)}$; the full expression can be found in section 5.

(23) Aveyard, R.; Binks, B. P.; Clint, J. H.; Fletcher, P. D. I.; Horozov, T. S.; Neumann, B.; Paunov, V. N.; Annesley, J.; Botchway, S. W.; Nees, D.; Parker, A. W.; Ward, A. D.; Burgess, A. *Phys. Rev. Lett.* **2002**, *88*, 246102-1-4.

(24) Horozov, T. S.; Aveyard, R.; Clint, J. H.; Binks, B. P. *Langmuir* **2003**, *19*, 2822.

(25) Kirkwood, J. G.; Buff, F. P. *J. Chem. Phys.* **1949**, *17*, 338.

(26) Felderhof, B. U. *J. Chem. Phys.* **1968**, *49*, 44.

(27) Poptoshev, E.; Rutland, M. W.; Claesson, P. M. *Langmuir* **1999**, *15*, 7789.

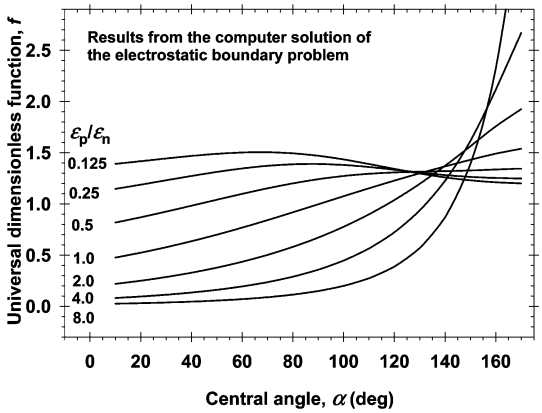

Figure 4. Plot of the universal function f in eq 3.4 vs the angle α for various ϵ_p/ϵ_n values denoted in the figure. f determines the magnitude of the force, $F^{(n)}$, which is due to the electric charges at the particle−nonpolar fluid boundary. For the particle in Figure 2, we have $\epsilon_p/\epsilon_n = 1.95$ and the central angle is $\alpha = 102°$; the corresponding value of f is 0.807. Using data tabulated in the Appendix, one can reproduce numerically the curves in the figure.

3.3. The Normal Balance of Forces Exerted on the Particle. This balance reads

$$2\pi r_c \gamma \sin\psi = F = F^{(w)} + F^{(n)} + F^{(g)} \qquad (3.5)$$

where $F^{(g)}$ is the contribution of gravity; see eq 2.1. Combining eqs 3.2−3.5, we obtain

$$\sin\psi = \frac{p \sin\alpha}{2\gamma\kappa} + \frac{\sigma_{pn}^2 \beta f}{2\pi\gamma\epsilon_0\epsilon_n} R + \frac{F^{(g)}}{2\pi\gamma r_c} \qquad (3.6)$$

where $\beta = (1 - \cos\alpha)/\sin\alpha$. The first term on the right-hand side of eq 3.6, which is independent of R, originates from the electric field in the water phase and depends on the electrolyte concentration, C, through κ. The second term, accounting for the electric charges at the particle−oil interface, is independent of C; it grows proportionally to the particle radius, R, and could dominate ψ for $R = 200-300\ \mu$m, as indicated by our experiments (see Figure 3 and the related discussion). The last, gravitational term in eq 3.6 is proportional to R^2, and it dominates ψ for millimeter-sized (and larger) particles. Additional results about the relative importance of $F^{(g)}$, $F^{(n)}$, and $F^{(w)}$ are given in section 3.7.

3.4. Electric Pressure Difference across the Fluid Interface. As mentioned above, to determine theoretically $F^{(n)}$ and $f(\alpha, \epsilon_p/\epsilon_n)$ (see eq 3.4 and Figure 4), we solved numerically the electrostatic boundary problem (section 5) for the case of a small meniscus slope ($\sin^2\psi \ll 1$) and a thin electric double layer in the aqueous phase ($\kappa R < 1$). Once the numerical solution is obtained, one can calculate also the electric pressure difference across the oil−water (or air−water) interface, p_{el}. We found that the obtained numerical data for $p_{el}(r)$ can be described, almost perfectly, by the following semiempirical expression (section 6):

$$p_{el}(r) = -\frac{2\lambda {r_c}^4 F^{(el)}}{\pi (r - r_c)^{1-\mu} r^{5+\mu}} \qquad (3.7)$$

$$\lambda = (3 + \mu)(2 + \mu)(1 + \mu)\mu/24 \qquad (3.8)$$

where, as usual, r is the radial coordinate (Figure 1) and $0 < \mu < 1$. In general, the parameter μ depends on the contact angle, θ, and on the ratio of the two dielectric constants: $\mu = \mu(\theta, \epsilon_p/\epsilon_n)$. On the other hand, μ is independent of σ_{pn} and R. For example, for the particle in Figure 2, from the fit of the numerical data for $p_{el}(r)$, we obtained $\mu = 0.690$, which, in view of eq 3.8, yields $\lambda = 0.482$. Equation 3.7 is applicable for $50° \le \theta \le 130°$. In the Appendix, we present numerical data for the function $\mu(\theta, \epsilon_p/\epsilon_n)$ as well as a convenient way to obtain the values of this function by polynomial interpolation.

For large distances from the particle, the asymptotic form of eq 3.7 reads

$$p_{el}(r) \approx -\frac{2\lambda {r_c}^4 F^{(el)}}{\pi r^6} \qquad (r/r_c \gg 1) \qquad (3.9)$$

This is in agreement with the estimate in ref 8 that asymptotically $p_{el} \propto 1/r^6$.

3.5. Particles at the Horizontal Fluid Interface: Meniscus Shape and Capillary Force. The profile of the oil−water (air−water) interface, $\zeta(r)$, obeys the Laplace equation of capillarity, which (in the considered case of a small meniscus slope) reduces to[2,3,6]

$$\frac{1}{r}\frac{d}{dr}\left(r\frac{d\zeta}{dr}\right) - q^2\zeta = \frac{1}{\gamma}p_{el} \qquad (3.10)$$

As before, $q^2 = \Delta\rho g/\gamma$. Note that, in the absence of any particle, the interface is a horizontal plane, thanks to the action of gravity. The terms with q^2 and p_{el} in eq 3.10 account, respectively, for the contributions of the gravitational and electric forces to the pressure difference across the fluid interface. Equation 3.10 represents an inhomogeneous modified Bessel equation, whose solution can be expressed in the following general form:[28]

$$\zeta = I_0(qr)\int_{r_c}^{r}\frac{p_{el}}{\gamma}K_0(q\hat{r})\hat{r}\,d\hat{r} - K_0(qr)\int_{r_c}^{r}\frac{p_{el}}{\gamma}I_0(q\hat{r})\hat{r}\,d\hat{r} + AK_0(qr) \qquad (3.11)$$

where I_0 and K_0 are the modified Bessel functions of the first and second kind and $\hat{r}$ and A are the integration variable and constant. A boundary condition at the contact line is

$$d\zeta/dr \approx \sin\psi = F/(2\pi\gamma r_c) \quad \text{at} \quad r = r_c \qquad (3.12)$$

For sufficiently small particles, including our glass spheres (Tables 1 and 2), we have $(qr_c)^2 \ll 1$, and then we can use the asymptotic expressions for I_0 and K_0:[29−31]

$$I_0(qr) \approx 1 \quad \text{and} \quad K_0(qr) \approx -\ln(\gamma_e qr/2) \quad \text{for} \quad (qr)^2 \ll 1 \qquad (3.13)$$

where, as before, γ_e is the Euler−Masceroni constant [$\ln(\gamma_e) = 0.577...$]. With the help of eqs 3.12 and 3.13, one can represent eq 3.11 in the form

(28) Kamke, E. *Differential Equations. Solution Methods and Solutions*; Teubner: Stuttgart, Germany, 1983.
(29) Janke, E.; Emde, F.; Lösch, F. *Tables of Higher Functions*; McGraw-Hill: New York, 1960.
(30) Dwight, H. B. *Tables of Integrals and Other Mathematical Data*; Macmillan Co.: New York, 1961.
(31) Abramowitz, M.; Stegun, I. A. *Handbook of Mathematical Functions*; Dover: New York, 1965.

$$\zeta = \frac{1}{\gamma}\int_{r_c}^{r}\frac{dr_2}{r_2}\int_{r_c}^{r_2} p_{el} r_1\, dr_1 + \frac{F}{2\pi\gamma}\ln\left(\frac{r}{r_0}\right) \quad \text{for} \quad (qr)^2 \ll 1 \tag{3.14}$$

where r_0 is a constant and r_1 and r_2 are integration variables; p_{el} is to be substituted from eq 3.7. An approximate form of eq 3.14 can be obtained if the asymptotic expression, eq 3.9, is substituted for p_{el}:

$$\zeta(r) = -\frac{\lambda F^{(el)}}{8\pi\gamma}\frac{r_c^4}{r^4} + \left(\frac{F - \lambda F^{(el)}}{2\pi\gamma}\right)\ln(r/r_0) \tag{3.15}$$

For $\lambda = F/F^{(el)} \approx 1$, eq 3.15 reduces to the respective expression in ref 13. If this were the case, the logarithmic term (which gives rise to the long-range capillary attraction[8]) would disappear. However, our experimental data for ζ versus $\log(r)$ (inset in Figure 2) show a well-pronounced linear portion (confirming the presence of the log term in eq 3.15) from whose slope we determine $\lambda = 0.484$. ($F^{(el)}$, obtained from eq 2.5, is given in Table 1.) The latter value of λ is very close to $\lambda = 0.482$, calculated from eq 3.8 with the theoretically computed value of μ; see section 3.4. The small difference between the two values of λ is probably due to the approximate character of the used eq 3.9. For the same reason, eq 3.15 is not accurate for $r \to r_c$; to describe quantitatively the meniscus shape very close to the particle, one should use eq 3.14 along with eq 3.7 and solve the integrals numerically.

For a small meniscus slope, we can express the energy of capillary interaction between two particles, $U(r)$, using the superposition approximation,[1,2,6,32] which gives $U(r) = F\zeta(r)$. Thus, from eq 3.15 we obtain

$$U(r) = -\frac{\lambda F F^{(el)}}{8\pi\gamma}\frac{r_c^4}{r^4} - \frac{F}{2\pi\gamma}(F - \lambda F^{(el)})\ln(r_0/r) \tag{3.16}$$

Hence, at not-too-small distances, $U(r)$ is dominated by the logarithmic term, which gives rise to a long-range attraction, as detected in ref 8. In other words, it turns out that Nikolaides et al.[8] are right to attribute the experimentally observed attraction to the long-range log term in $U(r)$. Moreover, the effect of the electric field on the meniscus shape (the effect of p_{el}) leads to the appearance of an additional short-range attractive term ($\propto 1/r^4$) in eq 3.16. Let us recall that the direct electrostatic repulsion between the two like-charged particles[8,23,24] also contributes to the total interaction energy, but this effect is not a subject of the present article.

Finally, we should note again that, because of the use of the approximate eq 3.9, the first term on the right-hand side of eq 3.16 is not accurate for $r \to r_c$. For quantitatively accurate results, one can use the expression

$$U(r) = \frac{F}{\gamma}\int_{r_c}^{r}\frac{dr_2}{r_2}\int_{r_c}^{r_2} p_{el} r_1\, dr_1 - \frac{F^2}{2\pi\gamma}\ln\left(\frac{r_0}{r}\right) \quad \text{for} \quad (qr)^2 \ll 1 \tag{3.17}$$

which follows from eq 3.14, with p_{el} given by eq 3.7; the integrals have to be solved numerically.

3.6. Particle at the Surface of a Spherical Drop. In fact, Nikolaides et al.[8] detected the long-range attractive force between particles at the surface of a spherical emulsion drop, for which the effects of the gravity force are certainly negligible. Then, a question arises of whether there will be a logarithmic term in the expressions for $\zeta(r)$ and $U(r)$ for the case of a spherical drop, as it is in eqs 3.14−3.17.

To answer this question, we will consider a particle that is much smaller than the emulsion drop, which corresponds to the experimental situation. Introducing spherical coordinates, $(\hat{\rho}, \hat{\theta}, \hat{\phi})$, one can express the meniscus shape around the particle in the form

$$\hat{\rho} = R_0 - \zeta(\hat{\theta}) \tag{3.18}$$

where R_0 is the radius of the spherical fluid interface (of the drop) in the hypothetic case when no electric (or other external) force is acting on the particle. (In the latter case, the forces, originating from the surface tension and the capillary pressure difference, exactly counterbalance each other for a spherical fluid interface; see, e.g., refs 6 and 32.) In this respect, ζ in eq 3.18 accounts for the deviation of the meniscus from the spherical shape due to the presence of a normal electric force exerted on the charged particle, as well as on the surrounding oil−water interface. For small deformations, $|\zeta/R_0| \ll 1$ and $|\nabla_s\zeta|^2 \ll 1$, where ∇_s is the surface gradient operator, the linearized Laplace equation of capillarity acquires the form[6,33,34]

$$\gamma\left(\frac{2}{R_0} + \frac{2\zeta}{R_0^2} + \nabla_s^2\zeta\right) = P_1 - P_2 + p_{el} \tag{3.19}$$

where P_1 and P_2 are the constant (independent of the spatial coordinates) pressures inside and outside the drop and p_{el} is the same as that in section 3.4. (If the effect of electric forces were missing, then $\zeta = 0$, $p_{el} = 0$, and eq 3.19 reduces to the familiar Laplace equation.) Equation 3.19 can be expressed in the following equivalent form:

$$\nabla_s^2\zeta + q^2\zeta = 2\Delta H + p_{el}/\gamma \qquad (q^2 = 2/R_0^2) \tag{3.20}$$

where $\Delta H = [(P_1 - P_2)/(2\gamma) - 1/R_0]$ is a constant. For a small particle, the configuration particle/interface looks like that in Figure 1, and one can use the same coordinates, (r, z), as those in the latter figure, to describe the meniscus shape; in such a case, eq 3.20 becomes

$$\frac{1}{r}\frac{d}{dr}\left(r\frac{d\tilde{\zeta}}{dr}\right) + q^2\tilde{\zeta} = \frac{1}{\gamma}p_{el} \tag{3.21}$$

where $\tilde{\zeta} = \zeta - 2q^{-2}\Delta H$. Note that eq 3.21 resembles eq 3.10, with the major difference being that the sign before q^2 is opposite and that the definitions of q in the two cases are also different. In analogy with eq 3.11, the solution of eq 3.21 can be expressed in the following general form:

$$\tilde{\zeta} = \frac{\pi}{2}Y_0(qr)\int_{r_c}^{r}\frac{p_{el}}{\gamma}J_0(q\hat{r})\hat{r}\, d\hat{r} - \frac{\pi}{2}J_0(qr)\int_{r_c}^{r}\frac{p_{el}}{\gamma}Y_0(q\hat{r})\hat{r}\, d\hat{r} + AY_0(qr) + BJ_0(qr) \tag{3.22}$$

where J_0 and Y_0 are the Bessel functions of the first and second kind and A and B are integration constants. The asymptotic expressions for J_0 and Y_0 are[29−31]

(32) Kralchevsky, P. A.; Nagayama, K. *Adv. Colloid Interface Sci.* **2000**, *85*, 145.

(33) Landau, L. D.; Lifshitz, E. M. *Fluid Mechanics*; Pergamon Press: Oxford, U.K., 1984.

(34) Kralchevsky, P. A.; Paunov, V. N.; Nagayama, K. *J. Fluid Mech.* **1995**, *299*, 105.

$$J_0(qr) \approx 1 \quad \text{and} \quad Y_0(qr) \approx \frac{2}{\pi}\ln\left(\frac{\gamma_e qr}{2}\right) \quad \text{for} \quad (qr)^2 \ll 1 \tag{3.23}$$

With the help of eq 3.23 and the boundary condition 3.12, the latter with $F = F^{(el)}$, we represent eq 3.22 in the form

$$\xi = \frac{1}{\gamma}\int_{r_c}^{r}\frac{dr_2}{r_2}\int_{r_c}^{r_2} p_{el} r_1\, dr_1 + \frac{F^{(el)}}{2\pi\gamma}\ln\left(\frac{\gamma_e qr}{2}\right) + B \quad \text{for} \quad (qr)^2 \ll 1 \tag{3.24}$$

Equation 3.24 can be easily represented in the form of eq 3.14, if the constant r_0 in the latter equation is redefined to include the multiplier $\gamma_e q/2$ and the additive constants B and $2q^{-2}\Delta H$, the latter coming from the definition of ξ; see eq 3.21. In other words, eqs 3.14−3.17, and the conclusion drawn from them, are valid also in the case of particles at the surface of a spherical drop. The only consequence of the absence of gravitational force for a spherical drop is that the total normal force becomes identical with the electrodipping force; that is, one has to substitute $F = F^{(el)}$ everywhere in eqs 3.14−3.17.

3.7. Numerical Results and Discussion. The theoretical expressions derived in the present article can be applied to a wide range of particle sizes, not only to the 200−300 μm beads in our experiments (section 2). As an example, let us consider the energy of capillary interaction, $U(r)$, between two identical particles of radius R, which are attached to a horizontal fluid interface. To obtain numerical results, we have to first determine the additive constant in eqs 3.15 and 3.16, which is related to the term $\ln(r_0)$. For this purpose, we can apply the method of the matched "inner" and "outer" asymptotic expansions.[35] Equation 3.15 represents the inner asymptotics (valid close to the contact line). The outer asymptotics are $\xi \propto K_0(qr)$, that is, the solution of eq 3.10 for negligible p_{el}. Matching the inner and outer asymptotics, in accordance with the Prandtl procedure,[35] yields $r_0 = 2/(\gamma_e q)$. Further, following the standard procedure in ref 35, we obtain generalized versions of eqs 3.15 and 3.16 in the form of "compound" solution:

$$\zeta(r) = -\frac{\lambda F^{(el)}}{8\pi\gamma}\frac{r_c^4}{r^4} - \left(\frac{F - \lambda F^{(el)}}{2\pi\gamma}\right)K_0(qr) \tag{3.25}$$

$$U(r) = -\frac{\lambda F F^{(el)}}{8\pi\gamma}\frac{r_c^4}{r^4} - \frac{F}{2\pi\gamma}(F - \lambda F^{(el)})K_0(qr) \tag{3.26}$$

The additive constant in eq 3.26 is determined in such a way that $U(r) \to 0$ for $r \to \infty$. If the particle has no electric charge, that is, $F^{(el)} = 0$, then eq 3.26 reduces to the known expression $U = -[F^2 K_0(qr)]/(2\pi\gamma)$ for the energy of capillary attraction between two floating heavy particles ($F = F^{(g)}$).[2,6,32] In the limit $qr \ll 1$, eqs 3.25 and 3.26 reduce, respectively, to eqs 3.15 and 3.16; see also eq 3.13.

Here, our aim is to compare the relative contributions in $U(r)$ of the gravity force, $F^{(g)}$, of the electric force at the particle−nonpolar fluid boundary, $F^{(n)}$, and of the electric force at the particle−water boundary, $F^{(w)}$. To do that, we will use parameter values for the experimental systems in section 2.

Thus, for the central angle, we use typical experimental values, $\alpha = 102$ and 117°, respectively, for the oil−water and air−water interfaces. To calculate $F^{(g)}$ from eq 2.1, we use $\rho_p = 2.62$ g/cm^3, $\rho_w = 1$ g/cm^3, and $\rho_n = 0.763$ for the oil phase. The corresponding dielectric constants are $\epsilon_p = 3.97$, $\epsilon_w = 80.1$, and $\epsilon_n = 2.04$. To calculate $F^{(n)}$ from eq 3.4, we use average values of the surface charge density from Tables 1 and 2, $\sigma_{pn} = 70.4$ and 25.7 μC/m^2, respectively, for the particle−oil and particle−air interfaces. Finally, to calculate $F^{(w)}$ from eqs 3.2 and 3.3, we specify $C = 5 \times 10^{-5}$ M ($\kappa^{-1} = 43.0$ nm) and $\sigma_{pw} = 1780\ \mu$C/m^2 (90 nm^2 per surface charge).[27] We recall that $F^{(g)} \propto R^3$ and $F^{(n)} \propto R^2$, while $F^{(w)} \propto R$.

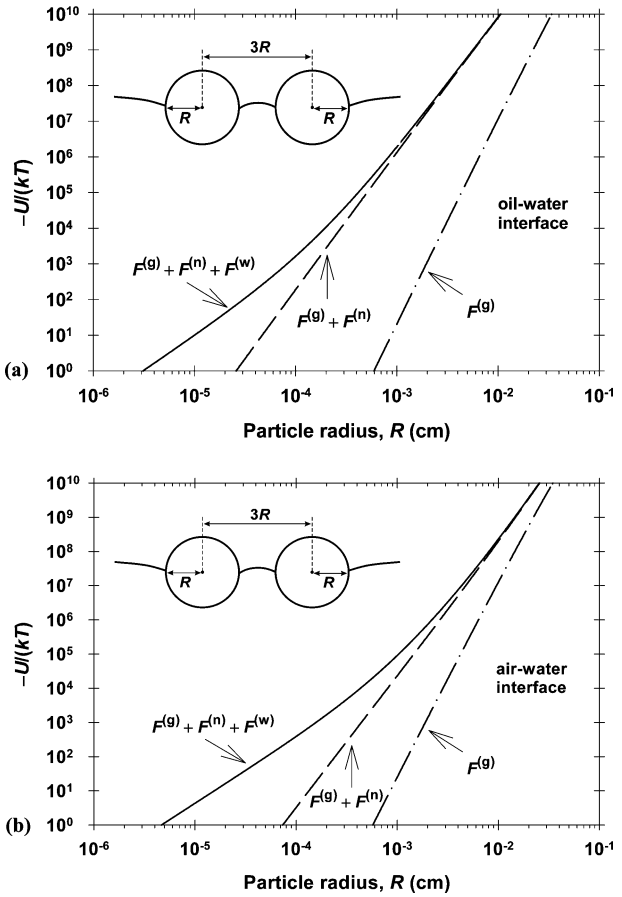

Figure 5. Dependence of the energy of lateral capillary attraction, U, on the particle radius, R, calculated from eq 3.26 for two particles separated at a center-to-center distance of $r = 3R$ (see the inset). U is scaled by the thermal energy, kT. (a) Oil−water interface. (b) Air−water interface. The parameter values are specified in the text. The three curves correspond to $F = F^{(g)}$, $F = F^{(g)} + F^{(n)}$, and $F = F^{(g)} + F^{(n)} + F^{(w)}$, as denoted in the figure.

In Figure 5, we illustrate how the energy of lateral capillary attraction between two identical spherical particles depends on their radius, R. We show plots of $U(r = 3R)$ versus R calculated by means of eq 3.26. Parts a and b of Figure 5 represent results for the oil−water and air−water interfaces, respectively. The dashed−dotted line is calculated for $F = F^{(g)}$ and corresponds to the case when the interfacial deformations are due only to the gravitational effect (particle weight and buoyancy force). In this case, for $R < 6\ \mu$m, the capillary interaction becomes negligible: $-U/kT < 1$.

The dashed lines in Figure 5a and b are calculated for $F = F^{(g)} + F^{(n)}$. Physically, this corresponds to larger particles (section 2) or to sufficiently high electrolyte concentrations, C, in the water phase, which lead to a negligible $F^{(w)}$ value. Now, due to the effect of $F^{(n)}$, the capillary attraction is considerably stronger than that in the previous case (see the dashed and dashed−dotted lines). The effect of $F^{(n)}$ is greater for the oil−water

(35) Nayfeh, A. H. *Perturbation Methods*; Wiley: New York, 1973.

Table 3. Values of the Particle Radius, R^*, for Which $F^{(n)} = F^{(w)}$, $F^{(g)} = F^{(w)}$, or $F^{(g)} = F^{(n)}$

interface	$F^{(n)} = F^{(w)}$ R^* (μm)	$F^{(g)} = F^{(w)}$ R^* (μm)	$F^{(g)} = F^{(n)}$ R^* (mm)
oil−water	1.37	69.5	3.50
air−water	7.18	54.0	0.411

interface. In particular, for $F = F^{(g)} + F^{(n)}$, the capillary attraction becomes significant ($-U/kT > 1$) at $R > 300$ and 800 nm, respectively, for the oil−water and air−water interfaces.

Finally, the solid lines in Figure 5a and b are calculated for $F = F^{(g)} + F^{(n)} + F^{(w)}$. In this case, thanks to the effect of $F^{(w)}$, the lateral capillary attraction becomes significant even for particles of radius $R = 40-50$ nm. Figure 5a indicates that, for an emulsion system (like that in ref 8) at $R \approx 1\ \mu$m, we have comparable contributions from $F^{(n)}$ and $F^{(w)}$. In contrast, for the air−water interface, the contribution of $F^{(w)}$ is predominant at $R \approx 1\ \mu$m.

In Table 3, we give the special value, R^*, of the particle radius for which $F^{(n)} = F^{(w)}$. For $R > R^*$, we have $F^{(n)} > F^{(w)}$, whereas, for $R < R^*$, we have $F^{(n)} < F^{(w)}$. Analogous values of R^* are given for the cases $F^{(g)} = F^{(w)}$ and $F^{(g)} = F^{(n)}$. The data in Table 3, which are calculated for the same parameter values as those in Figure 5, indicate which force for which particle sizes is predominant. In particular, it is impressive that we have $F^{(g)} > F^{(n)}$ for $R > 3.5$ mm; that is, the electric force $F^{(n)}$ can be significant even for millimeter-sized particles.

Of course, the data in Figure 5 and Table 3 depend on the specific choice of the parameter values. If we use a greater surface charge density, σ_{pw}, at the particle−water interface and a lower ionic strength, $C < 5 \times 10^{-5}$ M, in the water, then the magnitude of $F^{(w)}$ would increase and the capillary attraction could become significant even for particles of radii $R < 40-50$ nm. However, for such small particles and low ionic strengths, R becomes comparable to κ^{-1}, and consequently, eq 3.2 cannot be used to calculate $F^{(w)}$. In the latter case, one has to apply a numerical solution of the electrostatic problem; see section 5.3 below.

4. Electric Force at the Particle−Water Boundary

In this section, we derive eqs 3.2 and 3.3, which allow one to calculate the electric force $F^{(w)}$. Because of the theoretical character of our considerations, in sections 4−6, it is convenient to use the CGSE system of units.[36] In these units, the general expression for the Maxwell pressure tensor, $\mathbf{P}$, in an electric double layer reads[6,26]

$$\mathbf{P} = \left(P_o + \frac{\epsilon_w}{8\pi}E^2\right)\mathbf{U} - \frac{\epsilon_w}{4\pi}\mathbf{EE} \qquad (4.1)$$

where $\mathbf{E} = -\nabla\varphi$ is the electric field intensity, φ is the electric potential, $E^2 = \mathbf{E}\cdot\mathbf{E}$; $\mathbf{U}$ is the unit tensor; and P_o is the osmotic pressure.

$$P_o = P_\infty + kT\sum_i a_{i\infty}\left[\exp\left(-\frac{Z_i e\varphi}{kT}\right) - 1\right] \qquad (4.2)$$

P_∞ is the pressure in the bulk; the summation is carried out over all ionic species; Z_i is their valence; $a_{i\infty} = \gamma_{\pm}c_{i\infty}$ are the bulk activities of the ions, whose bulk concentrations are $c_{i\infty}$; and $\gamma_{\pm}$ is the activity coefficient.

(36) Landau, L. D.; Lifshitz, E. M. *Electrodynamics of Continuous Medium*; Pergamon Press: Oxford, U.K., 1960.

Let us consider a charged sphere in the bulk of an electrolyte solution. Because of the spherical symmetry, we have $\mathbf{E} = \mathbf{e}_r E_r = -\mathbf{e}_r\ \partial\varphi/\partial r$, where r is the radial coordinate and $\mathbf{e}_r$ is the respective unit vector. Substituting the latter expression in eq 4.1, in view of eq 4.2, one can check that the condition for mechanical equilibrium, $\nabla\cdot\mathbf{P} = 0$, which is equivalent to eq 3.1, gives

$$\frac{\partial^2\varphi}{\partial r^2} + \frac{2}{r}\frac{\partial\varphi}{\partial r} = -\frac{4\pi}{\epsilon_w}\sum_i Z_i e a_{i\infty}\exp\left(-\frac{Z_i e\varphi}{kT}\right) \qquad (4.3)$$

which is a form of the Poisson−Boltzmann equation. From eq 4.1, the following expressions for the normal and tangential components of the pressure tensor follow:

$$P_N \equiv P_{rr} = P_o - \frac{\epsilon_w}{8\pi}\left(\frac{d\varphi}{dr}\right)^2 \quad P_T = P_o + \frac{\epsilon_w}{8\pi}\left(\frac{d\varphi}{dr}\right)^2 \qquad (4.4)$$

Substituting eq 4.4 into eq 3.1 and integrating, we derive

$$\Delta P_N = P_N(\infty) - P_N(R) = \frac{\epsilon_w}{2\pi}\int_R^\infty\left(\frac{d\varphi}{dr}\right)^2\frac{dr}{r} \qquad (4.5)$$

Equation 4.5 shows that $\Delta P_N > 0$, which means that the pressure in the bulk of the solution is greater than that at the surface of the charged particle. For a thin electric double layer, that is, for $\kappa R \gg 1$, one can prove that

$$\Delta P_N \approx \frac{\epsilon_w}{2\pi R}\int_R^\infty\left(\frac{d\varphi}{dr}\right)^2 dr \approx \frac{16kTC}{\kappa R}\left[\cosh\left(\frac{e\varphi_{pw}}{2kT}\right) - 1\right] \qquad (4.6)$$

where φ_{pw} is the electric potential at the particle−water boundary; as before, C is the bulk concentration of a 1:1 electrolyte; and, at the last step, eq 4.3 has been also employed (details in refs 6 and 37). The Gouy equation, connecting the surface charge, σ_{pw}, and potential, φ_{pw}, for an electric double layer reads[6,36,38]

$$\sigma_{pw} = \frac{4eC}{\kappa}\sinh\left(\frac{e\varphi_{pw}}{2kT}\right) \qquad (\kappa R \gg 1) \qquad (4.7)$$

Finally, eliminating φ_{pw} between eqs 4.6 and 4.7 and using the relationship $F^{(w)} = \pi r_c^2\Delta P_N$, we obtain eqs 3.2 and 3.3.

5. Electric Force at the Particle−Oil Boundary

5.1. Basic Equations. The electrostatic boundary conditions at the particle−water and nonpolar fluid−water interfaces can be expressed in the form

$$\epsilon_p\frac{\partial\varphi_p}{\partial n} - \epsilon_w\frac{\partial\varphi_w}{\partial n} = 4\pi\sigma_{pw}$$
$$\epsilon_n\frac{\partial\varphi_n}{\partial n} - \epsilon_w\frac{\partial\varphi_w}{\partial n} = 4\pi\sigma_{nw} \qquad (5.1)$$

Here, we use the standard notation $\partial/\partial n$ for the directional derivative along the normal to the respective surface; as before, the subscripts "p", "w", and "n" refer to "particle", "water", and "nonpolar fluid" (oil, air, etc.); σ_{pw} and σ_{nw} are the surface charge densities at the respective phase boundaries. For a thin electric double layer in water, κR

(37) Kralchevsky, P. A.; Danov, K. D.; Broze, G.; Mehreteab, A. *Langmuir* **1999**, *15*, 2351.
(38) Gouy, G. *J. Phys. Radium* **1910**, *9*, 457.

$\gg 1$, the term proportional to ϵ_w, is predominant, and then, eq 5.1 reduces to

$$-\epsilon_w \frac{\partial \varphi_w}{\partial n} = 4\pi\sigma_{pw} \quad -\epsilon_w \frac{\partial \varphi_w}{\partial n} = 4\pi\sigma_{nw} \quad (\kappa R \gg 1) \quad (5.2)$$

In principle, eq 5.2 allows one to solve the Poisson−Boltzmann equation in the water phase and to determine the $\varphi_w(\mathbf{r})$ value for given σ_{pw} and σ_{nw} values. Then, at a second step, the values of φ_w at the particle−water and nonpolar fluid−water interfaces can be computed and used as boundary conditions for the Poisson equation in the nonpolar fluid and inside the particle. The surface potentials can be calculated from the following equations:

$$\sinh\left(\frac{\Phi_{pw}}{2}\right) = \frac{\kappa\sigma_{pw}}{4eC} \qquad \sinh\left(\frac{\Phi_{nw}}{2}\right) = \frac{\kappa\sigma_{nw}}{4eC} \quad (5.3)$$

In eq 5.3, and below, we use dimensionless electric potentials:

$$\Phi_w \equiv \frac{e\varphi_w}{kT} \qquad \Phi_p \equiv \frac{e\varphi_p}{kT} \qquad \Phi_n \equiv \frac{e\varphi_n}{kT} \quad (5.4)$$

For a thin electric double layer ($\kappa R \gg 1$), we have the following boundary conditions:

$$\Phi_p = \Phi_{pw} = \text{constant at } S_{pw} \quad \text{and}$$
$$\Phi_n = \Phi_{nw} = \text{constant at } S_{nw} \quad (5.5)$$

where the surfaces S_{pw} and S_{nw} represent the respective phase boundaries. At the particle−nonpolar fluid interface, we will use the boundary condition

$$\left(\frac{\epsilon_p}{\epsilon_n}\tilde{\nabla}\Phi_p - \tilde{\nabla}\Phi_n\right)\cdot\mathbf{n} = \frac{4\pi e}{kT\epsilon_n} r_c \sigma_{pn} \quad (5.6)$$

where $\tilde{\nabla} \equiv r_c\nabla$ and $\mathbf{n}$ is the outer unit normal to the particle surface. The electric field in the nonaqueous phases (particle and oil) depends on three constant parameters, Φ_{pw}, Φ_{nw}, and σ_{pn}, which enter the boundary conditions 5.5 and 5.6. Because we are dealing with a linear boundary problem, its solution inside the particle, Φ_p, and inside the nonpolar fluid, Φ_n, can be presented as a superposition of two functions, Φ^φ and Φ^σ, which satisfy the boundary conditions shown in parts a and b of Figures 6, respectively:

$$\Phi_p \equiv \Phi_{nw} + (\Delta\Phi)\Phi_p^\varphi + \frac{4\pi e}{kT\epsilon_n} r_c \sigma_{pn} \Phi_p^\sigma \quad (5.7)$$

$$\Phi_n \equiv \Phi_{nw} + (\Delta\Phi)\Phi_n^\varphi + \frac{4\pi e}{kT\epsilon_n} r_c \sigma_{pn} \Phi_n^\sigma \quad (5.8)$$

where $\Delta\Phi = \Phi_{pw} - \Phi_{nw}$. All the functions, Φ_p^φ, Φ_n^φ, Φ_p^σ, and Φ_n^σ, obey the Laplace equation, $\nabla^2\Phi = 0$. The boundary conditions for the functions Φ_p^φ and Φ_n^φ, which are illustrated in Figure 6a, are

$$\Phi_p^\varphi = 1 \text{ at } S_{wp} \qquad \Phi_n^\varphi = 0 \text{ at } S_{nw} \quad (5.9)$$

$$\left(\frac{\epsilon_p}{\epsilon_n}\tilde{\nabla}\Phi_p^\varphi - \tilde{\nabla}\Phi_n^\varphi\right)\cdot\mathbf{n} = 0 \quad \Phi_p^\varphi = \Phi_n^\varphi \text{ at } S_{pn} \quad (5.10)$$

The boundary conditions for Φ_p^σ and Φ_n^σ, which are illustrated in Figure 6b, are

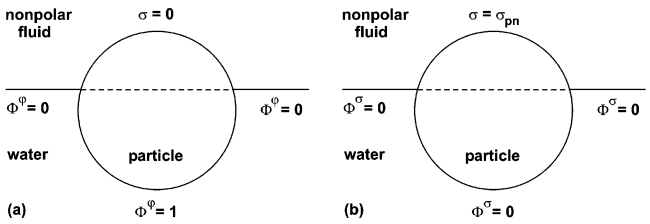

Figure 6. Two auxiliary boundary problems: (a) The functions Φ_p^φ and Φ_n^φ satisfy the boundary condition $\Phi^\varphi = 1$ at the particle−water interface, while the surface charge is $\sigma = 0$ at the particle−nonpolar fluid interface. (b) The functions Φ_p^σ and Φ_n^σ correspond to a nonzero surface charge at the particle−nonpolar fluid interface, $\sigma = \sigma_{pn}$, while the potential Φ^σ is zero at the particle−water interface. In both cases, the potential is zero at the particle−nonpolar fluid interface.

$$\Phi_p^\sigma = 0 \text{ at } S_{pw} \qquad \Phi_n^\sigma = 0 \text{ at } S_{nw} \quad (5.11)$$

$$\left(\frac{\epsilon_p}{\epsilon_n}\tilde{\nabla}\Phi_p^\sigma - \tilde{\nabla}\Phi_n^\sigma\right)\cdot\mathbf{n} = 1 \quad \Phi_p^\sigma = \Phi_n^\sigma \text{ at } S_{pn} \quad (5.12)$$

In view of eqs 4.1 and 5.4, the electric force $\mathbf{F}^{(n)}$, acting on the particle from the nonpolar fluid, can be expressed in the form

$$\mathbf{F}^{(n)} = \frac{\epsilon_n}{4\pi}\left(\frac{kT}{e}\right)^2 \int_{S_{pn}} \left[\nabla\tilde{\Phi}_n \nabla\tilde{\Phi}_n - \frac{1}{2}(\nabla\tilde{\Phi}_n)^2\mathbf{U}\right]\cdot\mathbf{n}\, d\tilde{S} \quad (5.13)$$

where $d\tilde{S}$ is a dimensionless surface element, scaled with r_c^2. Substituting eqs 5.7 and 5.8 into eq 5.13, we derive

$$\mathbf{F}^{(n)} = -\left[\frac{\epsilon_n}{4\pi}(\Delta\varphi)^2 f_{\varphi\varphi} + 2r_c\sigma_{pn}(\Delta\varphi) f_{\varphi\sigma} + \frac{4\pi}{\epsilon_n} r_c^2 \sigma_{pn}^2 f_{\sigma\sigma}\right]\mathbf{e}_z \quad (5.14)$$

where $\Delta\varphi = (kT/e)\Delta\Phi$; the dimensionless functions $f_{\varphi\varphi}$, $f_{\varphi\sigma}$, and $f_{\sigma\sigma}$ depend only on the central angle, α, and on the ratio ϵ_p/ϵ_n. The latter three functions are defined as follows:

$$f_{\varphi\varphi} = -\mathbf{e}_z \cdot \int_{S_{pn}} \left[\tilde{\nabla}\Phi_n^\varphi \tilde{\nabla}\Phi_n^\varphi - \frac{1}{2}(\tilde{\nabla}\Phi_n^\varphi)^2\mathbf{U}\right]\cdot\mathbf{n}\, d\tilde{S} \quad (5.15)$$

$$f_{\varphi\sigma} = -\frac{1}{2}\mathbf{e}_z \cdot \int_{S_{pn}} [\tilde{\nabla}\Phi_n^\varphi \tilde{\nabla}\Phi_n^\sigma + \tilde{\nabla}\Phi_n^\sigma \tilde{\nabla}\Phi_n^\varphi - (\tilde{\nabla}\Phi_n^\varphi \cdot \tilde{\nabla}\Phi_n^\sigma)\mathbf{U}]\cdot\mathbf{n}\, d\tilde{S} \quad (5.16)$$

$$f_{\sigma\sigma} = -\mathbf{e}_z \cdot \int_{S_{pn}} \left[\tilde{\nabla}\Phi_n^\sigma \tilde{\nabla}\Phi_n^\sigma - \frac{1}{2}(\tilde{\nabla}\Phi_n^\sigma)^2\mathbf{U}\right]\cdot\mathbf{n}\, d\tilde{S} \quad (5.17)$$

Because the electric potentials satisfy the Laplace equation, $\nabla^2\Phi = 0$, in the nonpolar and particle phases, one can prove that $\nabla\cdot\mathbf{T} = \mathbf{0}$, where $\mathbf{T}$ is any of the tensors in the brackets in eqs 5.15−5.17. Then, with the help of the Gauss−Ostrogradsky theorem, we can represent eqs 5.15−5.17 as integrals over the water−nonpolar fluid interface, which in first approximation is considered to be flat:

$$f_{\varphi\varphi} = \pi\int_1^\infty \left(\frac{\partial\Phi_n^\varphi}{\partial\tilde{z}}\right)^2 \tilde{r}\, d\tilde{r} \qquad f_{\varphi\sigma} = \pi\int_1^\infty \frac{\partial\Phi_n^\varphi}{\partial\tilde{z}}\frac{\partial\Phi_n^\sigma}{\partial\tilde{z}}\tilde{r}\, d\tilde{r}$$
$$f_{\sigma\sigma} = \pi\int_1^\infty \left(\frac{\partial\Phi_n^\sigma}{\partial\tilde{z}}\right)^2 \tilde{r}\, d\tilde{r} \quad (5.18)$$

We have introduced the dimensionless coordinates $\tilde{r} = r/r_c$ and $\tilde{z} = z/r_c$. Equation 5.18 indicates that the

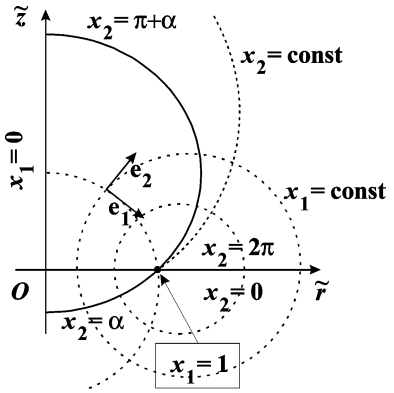

Figure 7. Orthogonal toroidal coordinates used in the numerical solution. $\tilde{z}$ is the axis of revolution. The coordinate surfaces x_1 = constant are toroids, while the surfaces x_2 = constant are spheres. In particular, the particle−water and particle−nonpolar fluid boundaries correspond to $x_2 = \alpha$ and $x_2 = \pi + \alpha$ ($\sin\alpha = r_c/R$); the water−nonpolar fluid interface corresponds to $x_2 = 2\pi$; the line of three-phase contact at the particle surface is at $x_1 = 1$.

dimensionless functions $f_{\varphi\varphi}$, $f_{\varphi\sigma}$, and $f_{\sigma\sigma}$ are always positive. Let us substitute typical parameter values to estimate the relative importance of the terms in eq 5.14: $\epsilon_n = 2$, $r_c = 200\ \mu$m, $\sigma_{pn} = 80\ \mu$C/m^2 (2000 nm^2 per charge), and $\Delta\varphi = 60$ mV. (Note that $\Delta\varphi$ in eq 5.14 must be substituted in CGSE units; i.e., the value of $\Delta\varphi$ in volts must be divided by 300.) Thus, we estimate the magnitude of the terms in eq 5.14:

$$F^{(n)} = [6.37 \times 10^{-9} f_{\varphi\varphi} + 1.92 \times 10^{-4} f_{\varphi\sigma} + 1.45 f_{\sigma\sigma}] \text{ (dynes)} \quad (5.19)$$

The term with $f_{\sigma\sigma}$ is the leading term in $F^{(n)}$. Finally, keeping only the last term in eq 5.14 and substituting $f_{\sigma\sigma} = (1 - \cos\alpha)\, f(\alpha, \epsilon_p/\epsilon_n)/\sin^2\alpha$, we obtain eq 3.4.

5.2. Numerical Solution. As already mentioned, the dimensionless potentials Φ_p^{φ}, Φ_n^{φ}, Φ_p^{σ}, and Φ_n^{σ} obey the Laplace equation:

$$\nabla^2\Phi_p^{\varphi} = 0 \quad \nabla^2\Phi_n^{\varphi} = 0 \quad \nabla^2\Phi_p^{\sigma} = 0 \quad \nabla^2\Phi_n^{\sigma} = 0 \quad (5.20)$$

To solve numerically the above equations, along with the respective boundary conditions (Figure 6), it is convenient to introduce the toroidal coordinates x_1 and x_2 (Figure 7):

$$\tilde{r} \equiv \frac{2x_1}{h} \qquad \tilde{z} \equiv \frac{x_1^2 - 1}{h}\sin x_2$$
$$h \equiv (x_1^2 + 1) + (x_1^2 - 1)\cos x_2 \quad (5.21)$$

In toroidal coordinates, the Laplace operator, ∇^2, acquires the form

$$\nabla^2\Phi = \frac{h^2}{4}\frac{\partial^2\Phi}{\partial x_1^2} + \frac{h^2}{(x_1^2 - 1)^2}\frac{\partial^2\Phi}{\partial x_2^2} + \left(\frac{h^2}{4x_1} + \frac{x_1 h}{x_1^2 - 1}\right)\frac{\partial\Phi}{\partial x_1} + \frac{h\sin x_2}{x_1^2 - 1}\frac{\partial\Phi}{\partial x_2} \quad (5.22)$$

The *boundary problem A*, corresponding to Figure 6a, is to solve the Laplace equations for Φ_p^{φ} and Φ_n^{φ}, along with the boundary conditions

$$\frac{\epsilon_p}{\epsilon_n}\frac{\partial\Phi_p^{\varphi}}{\partial x_2} - \frac{\partial\Phi_n^{\varphi}}{\partial x_2} = 0 \quad \text{at} \quad x_2 = \pi + \alpha \quad (5.23)$$

$$\Phi_p^{\varphi} = 1 \quad \text{at} \quad x_2 = \alpha \quad \Phi_n^{\varphi} = 0 \quad \text{at} \quad x_2 = 2\pi \quad (5.24)$$

The *boundary problem B*, corresponding to Figure 6b, is to solve the Laplace equations for Φ_p^{σ} and Φ_n^{σ}, along with the boundary conditions

$$\frac{\epsilon_p}{\epsilon_n}\frac{\partial\Phi_p^{\sigma}}{\partial x_2} - \frac{\partial\Phi_n^{\sigma}}{\partial x_2} = \frac{1 - x_1^2}{(x_1^2 + 1) - (x_1^2 - 1)\cos\alpha} \quad \text{at} \quad x_2 = \pi + \alpha \quad (5.25)$$

$$\Phi_p^{\sigma} = 0 \quad \text{at} \quad x_2 = \alpha \quad \Phi_n^{\sigma} = 0 \quad \text{at} \quad x_2 = 2\pi \quad (5.26)$$

To obtain numerical solution of the problem, we divided the rectangular area $[0, 1] \times [\alpha, \pi + \alpha]$, corresponding to the interior of the spherical particle, on 101 × 101 subdomains with steps $\Delta x_1 = 0.01$ and $\Delta x_{2p} = 0.01\pi$. The domain $[0, 1] \times [\pi + \alpha, 2\pi]$, corresponding to the nonpolar phase, is also divided on 101 × 101 subdomains with uniform steps $\Delta x_1 = 0.01$ and $\Delta x_{2n} = 0.01(\pi - \alpha)$. The respective derivatives in the Laplace operator, eq 5.22, are interpolated using second order difference schemes:

$$\frac{\partial\Phi_{i,j}}{\partial x_1} = \frac{\Phi_{i+1,j} - \Phi_{i-1,j}}{2\Delta x_1} \quad \text{and}$$
$$\frac{\partial^2\Phi_{i,j}}{\partial x_1^2} = \frac{\Phi_{i+1,j} - 2\Phi_{i,j} + \Phi_{i-1,j}}{(\Delta x_1)^2} \quad \text{with precision } (\Delta x_1)^2$$

$$\frac{\partial\Phi_{i,j}}{\partial x_2} = \frac{\Phi_{i,j+1} - \Phi_{i,j-1}}{2\Delta x_2} \quad \text{and}$$
$$\frac{\partial^2\Phi_{i,j}}{\partial x_2^2} = \frac{\Phi_{i,j+1} - 2\Phi_{i,j} + \Phi_{i,j-1}}{(\Delta x_2)^2} \quad \text{with precision } (\Delta x_2)^2$$

For the first derivatives in the boundary conditions, the second order backward and forward interpolation formulas are used; that is,

$$\frac{\partial\Phi_{i,j}}{\partial x_2} = \frac{3\Phi_{i,j} - 4\Phi_{i,j-1} + \Phi_{i,j-2}}{2\Delta x_2} \quad \text{and}$$
$$\frac{\partial\Phi_{i,j}}{\partial x_2} = \frac{-3\Phi_{i,j} + 4\Phi_{i,j+1} - \Phi_{i,j+2}}{2\Delta x_2}$$

with precision $(\Delta x_2)^2$. As a result, each of the two boundary problems (A and B) is reduced to a linear system of 20 301 equations for the values of the functions in each numerical node. The matrix of the system is spear. In our computer program, this matrix is solved exactly (no iterations or approximations) with the help of an upgraded version of the method for solving "band diagonal systems of equations"; see p 43 in ref 39.

The numerical solution gives the values of the functions Φ_p^{φ}, Φ_n^{φ}, Φ_p^{σ}, and Φ_n^{σ}. Further, the force coefficients in eq

(39) Press, W. H.; Teukolsky, S. A.; Vetterling, W. T.; Flannery, B. P. *Numerical Recipes in FORTRAN: The Art of Scientific Computing*, 2nd ed.; Cambridge University Press: Cambridge, U.K., 1992.

5.14 are calculated by using a version of eq 5.18 in toroidal coordinates:

$$f_{\varphi\varphi} = 4\pi\int_0^1 \left(\frac{\partial\Phi_n^{\varphi}}{\partial x_2}\right)^2 \frac{x_1}{(1-x_1^2)^2}\,dx_1$$

$$f_{\varphi\sigma} = 4\pi\int_0^1 \frac{\partial\Phi_n^{\varphi}}{\partial x_2}\frac{\partial\Phi_n^{\sigma}}{\partial x_2}\frac{x_1}{(1-x_1^2)^2}\,dx_1 \qquad (5.27)$$

$$f_{\sigma\sigma} = 4\pi\int_0^1 \left(\frac{\partial\Phi_n^{\sigma}}{\partial x_2}\right)^2 \frac{x_1}{(1-x_1^2)^2}\,dx_1 \qquad (5.28)$$

For the first derivatives in eqs 5.27 and 5.28, we again apply the second order backward interpolation formula (see above). The integrals are taken numerically, using the standard Simpson rule (five order precision), as given in ref 39, p 126. This scheme does not give an additional error because it is of higher order than the numerical scheme for solving the boundary problems A and B. In particular, from the computed $f_{\sigma\sigma}$ value, we determine the function f in eqs 3.4 and 3.6: $f = (\sin\alpha)^2 f_{\sigma\sigma}/(1-\cos\alpha)$.

5.3. Numerical Procedure for Calculations in the Case of $\kappa R \leq 1$. In this case, the procedure is similar to that described above (for $\kappa R \gg 1$). The main difference is that now the boundary problem for the electric field in the water phase cannot be separated from those in the other two phases (particle and nonpolar fluid). As a result, in the water phase, we have additionally 101 × 101 grid points, which increases the number of equations up to 30 401. The resulting linear system of equations can be solved exactly, by means of the same numerical method; see the text after eq 5.26.

6. Electric Force at the Water−Nonpolar Fluid Interface

6.1. Computation of the Meniscus Profile. The electric-field-induced pressure difference across the water−nonpolar fluid interface, p_{el}, is determined by the respective Maxwell stress:

$$p_{el} = P_{zz}^{(n)} = -\frac{\epsilon_n}{8\pi}\left(\frac{\partial\varphi_n}{\partial z}\right)^2 \approx -\frac{2\pi\sigma_{pn}^2}{\epsilon_n}\left[\frac{\partial\Phi_n^{\sigma}}{\partial x_2}\frac{2x_1^2}{x_1^2-1}\right]_{x_2=2\pi}^2 \qquad (6.1)$$

Note that, in the two boundary problems (Figure 6), the potential along the water−nonpolar fluid interface is constant, and therefore, only the z-derivative appears in eq 6.1. As in eq 5.19, the main contribution to Δp_{el} is that originating from the nonzero surface charge, σ_{pn}. For this reason, in eq 6.1, we keep only the leading term, proportional to σ_{pn}^2. In view of Figure 7, the oil−water (air−water) interface is described by $x_2 = 2\pi$ at varying x_1 values; in this case, $\tilde{r} = 1/x_1$.

In toroidal coordinates, the Laplace equation of capillarity, eq 3.10, acquires the form

$$\frac{\gamma}{r_c^2}\left(\frac{1}{x_1^4}\frac{\partial^2\zeta}{\partial x_1^2} - \frac{3}{x_1^5}\frac{\partial\zeta}{\partial x_1}\right) = p_{el} + (\rho_w - \rho_n)g(\zeta - \zeta_\infty) \qquad (6.2)$$

where $z = \zeta(x_1)$ is the deviation of the meniscus profile from planarity, the last term in eq 6.2 accounts for the gravitational hydrostatic pressure, ζ_∞ is the meniscus level at infinity, g is the acceleration due to gravity, and ρ_w and ρ_n are the mass densities of the respective phases. It turns out that, in the vicinity of the particle, the gravitational hydrostatic term in eq 6.2 is completely negligible and can be omitted. The theoretical curve in the inset in Figure 2 is computed by numerical solution of eq 6.2, at known p_{el} values, given by eq 6.1. In particular, eq 6.2 is represented as a system of two first order differential equations (for the function and its derivative), with known boundary conditions at the contact line. The latter system is solved numerically using the second order Runge−Kutta midpoint method given on p 704 in ref 39.

6.2. Analytical Expression for p_{el}. The numerical solution of the boundary problem along with eq 6.1 allowed us to calculate $p_{el}(r)$ curves for various parameter values. For all of them, the double logarithmic plots of p_{el} versus r represent parallel straight lines of slope −6 in the asymptotic case $r \to \infty$. Consequently, $p_{el} \propto 1/r^6$ for $r \to \infty$, as estimated in ref 8.

A useful relationship follows from the fact that at equilibrium the pressure tensor obeys the relationship $\nabla\cdot\mathbf{P} = 0$. For the nonpolar fluid, one can write

$$\int_{V_n} dV\,\nabla\cdot\mathbf{P}^{(n)} = \int_{S_{pn}} ds\,(-\mathbf{n})\cdot\mathbf{P}^{(n)} + \int_{S_{nw}} ds\,(-\mathbf{e}_z)\cdot\mathbf{P}^{(n)} \qquad (6.3)$$

Consequently,

$$-\mathbf{e}_z F^{(n)} \equiv \int_{S_{pn}} ds\,(-\mathbf{n})\cdot\mathbf{P}^{(n)} = \int_{S_{nw}} ds\,\mathbf{e}_z\cdot\mathbf{P}^{(n)} \qquad (6.4)$$

Likewise, for the water phase one can deduce

$$-\mathbf{e}_z F^{(w)} \equiv \int_{S_{pw}} ds\,(-\mathbf{n})\cdot\mathbf{P}^{(w)} = \int_{S_{nw}} ds\,(-\mathbf{e}_z)\cdot\mathbf{P}^{(w)} \qquad (6.5)$$

Summing up eqs 6.4 and 6.5, we obtain

$$F^{(el)} = -2\pi\int_{r_c}^{\infty} dr\; r p_{el}(r) \qquad (6.6)$$

where $F^{(el)} = F^{(n)} + F^{(w)}$ and $p_{el} = \mathbf{e}_z\cdot[\mathbf{P}^{(n)} - \mathbf{P}^{(w)}]\cdot\mathbf{e}_z$.

Having in mind the asymptotic behavior of $p_{el}(r)$, we search this function in the form

$$p_{el}(r) = \frac{A_1}{(r-r_c)^{1-\mu} r^{5+\mu}} \qquad (6.7)$$

where A_1 is a constant. Indeed, for $r \to \infty$, eq 6.7 gives $p_{el} \propto 1/r^6$. The unknown multiplier A_1 is determined by substituting eq 6.7 into eq 6.6. In this way, we get

$$A_1 = -\frac{2\lambda r_c^4 F^{(el)}}{\pi} \qquad (6.8)$$

where $\lambda = (3+\mu)(2+\mu)(1+\mu)\mu/24$. Thus, as a result, we obtain eq 3.7. We have used the integral[40,41]

$$\int_{r_c}^{\infty} r^{-\eta}(r-r_c)^{\mu-1}\,dr = r_c^{\mu-\eta}\,B(\eta-\mu,\mu) \quad (\eta > \mu > 0) \qquad (6.9)$$

(in our case, $\eta = 4 + \mu$). Here, B is the beta function; see, for example, refs 31, 41, and 42.

(40) Prudnikov, A. P.; Brychkov, Yu. A.; Marichev, O. I. *Integrals and Series, Vol. 1: Elementary Functions*; Gordon and Breach: New York, 1986.

(41) Gradshteyn, I. S.; Ryzhik, I. M. *Table of Integrals, Series, and Products*; 6th ed.; Academic Press: London, 2000.

(42) Korn, G. A.; Korn, T. M. *Mathematical Handbook*; McGraw-Hill: New York, 1968.

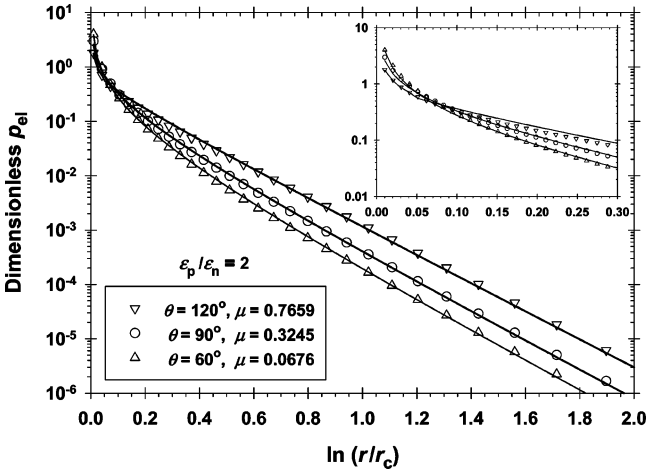

Figure 8. Plot of the dimensionless electric pressure, $\tilde{p}_{el}$, vs $\ln(r/r_c)$. The symbols are obtained by numerical solution of the electrostatic boundary problem, along with eqs 6.9−6.11, for three different values of θ denoted in the figure; for all curves, $\epsilon_p/\epsilon_n = 2$. The continuous lines are drawn by substituting eq 3.7 into eq 6.11; μ is an adjustable parameter determined from the best fit. The inset shows the upper left part of the curves in an enlarged scale.

6.3. Test of the Analytical Expression. Finally, to test eq 3.7 against the exact numerical solution, we represent eq 6.1 in the form

$$p_{el} \approx -\frac{2\pi\sigma_{pn}^2}{\epsilon_n}\left(\frac{\partial\Phi_n^{\sigma}}{\partial\tilde{z}}\right)^2_{x_2 = 2\pi} \qquad (6.10)$$

In addition, from eqs 5.14−5.19, we get

$$F^{(n)} \approx -\frac{4\pi^2}{\epsilon_n} r_c{}^2\sigma_{pn}^2\int_1^{\infty}\left(\frac{\partial\Phi_n^{\sigma}}{\partial\tilde{z}}\right)^2_{x_2 = 2\pi}\tilde{r}\,d\tilde{r} \qquad (6.11)$$

Having in mind that in our case $F^{(el)} \approx F^{(n)}$, we define the dimensionless p_{el} variable as follows:

$$\tilde{p}_{el} = -\frac{p_{el} r_c{}^2}{F^{(el)}} \approx -\frac{p_{el} r_c{}^2}{F^{(n)}} \qquad (6.12)$$

It turns out that the dimensionless electric pressure, $\tilde{p}_{el}$, as defined by eq 6.12, depends on a single parameter, μ: $\tilde{p}_{el} = \tilde{p}_{el}(r, \mu)$, where μ is the same as that in eq 6.7. In its own turn, μ depends on the angle θ and the ratio ϵ_p/ϵ_n but is independent of σ_{pn} and R.

Figure 8 illustrates the fit of numerical data for $\tilde{p}_{el}(r)$ with the analytical formula, eq 3.7. The three curves correspond to different values of the contact angle θ (60, 90, and 120°), while $\epsilon_p/\epsilon_n = 2$ is fixed. The symbols are calculated points, obtained by solving numerically the electrostatic boundary problem and using eqs 6.10 and 6.11. (The density of the computed points is greater than that shown in Figure 8, but we have plotted only a part of them to avoid overloading of the graph.) The continuous lines represent the best fits of the numerical data with eq 3.7, where μ has been determined as an adjustable parameter. Its values, corresponding to the fits, are given in the figure. One sees that the semiempirical eq 3.7 agrees very well with the numerical solution. Additional information about the computation of $\mu = \mu(\theta, \epsilon_p/\epsilon_n)$ can be found in the Appendix.

7. Summary and Conclusions

The reported experimental results (Tables 1 and 2, Figures 2 and 3) show that the interfacial deformation around glass particles ($R = 200-300\ \mu$m), situated at an oil−water (or air−water) interface, is dominated by the electrodipping force, $F^{(el)}$, rather than by gravity. The experimentally determined $F^{(el)}$ value (see eq 2.5 and the tables) does not depend on the NaCl concentration in the water phase. $F^{(el)}$ is greater for an oil−water interface than for an air−water interface.

Under our experimental conditions, $F^{(el)}$ is due to charges at the particle−oil (instead of particle−water) boundary. In other words, the integral electric force at the particle−oil interface, $F^{(n)}$, is much greater than the analogous force at the particle−water interface, $F^{(w)}$.

Theoretical expressions for $F^{(w)}$ and $F^{(n)}$ are derived (eqs 3.2 and 3.4), which indicate that each of these forces pushes the particle into water. From the experimentally determined $F^{(n)}$ value, which is practically equal to $F^{(el)}$, we calculated the surface charge density at the particle−oil (particle−air) interface, σ_{pn}; see Tables 1 and 2. The obtained values of σ_{pn} are constant (independent of the specific experiment) and are close to the values of σ_{pn} independently determined for a similar system.[24] On the other hand, irrespective of the much higher charge density at the particle−water interface, $\sigma_{pw} \gg \sigma_{pn}$, the electric force exerted on the latter boundary is much smaller, $F^{(w)} \ll F^{(n)}$; see section 3.1. However, $F^{(w)}$ can be important for smaller particles (50 nm < R < 1 μm); see section 3.7 and Figure 5.

The electrostatic boundary problem is reduced to an appropriate set of differential equations in toroidal coordinates, which is solved numerically. This approach enables us to compute exactly the electric forces acting on the particle−oil and oil−water interfaces; see sections 5 and 6.

Analytical expression for the electric pressure difference across the oil−water (air−water) interface, p_{el}, is obtained, eq 3.7, and tested against the exact numerical solution (Figure 8). Knowing p_{el}, we computed the shape of the liquid meniscus, $\zeta(r)$, using the experimental σ_{pn} value, determined from $F^{(el)}$. The experimental and computed profiles of $\zeta(r)$ are in excellent agreement (inset in Figure 2), without using any adjustable parameters. In particular, both the experimental and the calculated meniscus profile exhibit a logarithmic dependence, $\zeta(r) \propto \ln(r)$, at long distances from the particle. This result is in conformity with the explanation of the long-range interparticle attraction given by Nikolaides et al.[8] Deviation from the latter dependence is observed at short distances from the particle surface because of the effect of p_{el}; see eqs 3.14 and 3.15. Such an effect was discussed in refs 8 and 13. This effect leads to a short-range capillary attraction between two particles (eqs 3.16 and 3.17).

The above conclusions are valid not only for a large fluid interface, which is horizontal thanks to the action of gravity, but also for a spherical emulsion drop, whose shape is unaffected by gravity; see section 3.6. Expressions for the energy of capillary interaction between two particles are derived in the framework of the superposition approximation; see eq 3.17.

The electrodipping force, and the related long-range capillary attraction, can produce two-dimensional aggregation and self-assembly of colloid particles. These phenomena could be rather universal; they could appear for particles, whose characteristic size can be from dozens of nanometers to millimeters. The investigated effects could have important implications for colloid science and the development of new materials.[7,15−20]

Acknowledgment. We thank Professor Ivan B. Ivanov and Dr. Tommy Horozov for the helpful discussions, Dr.

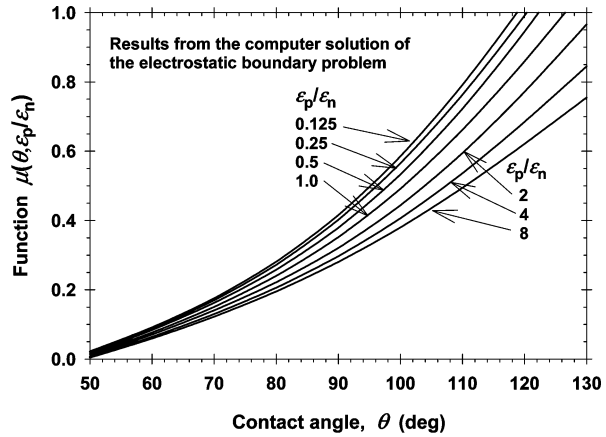

Figure 9. Plot of the universal function μ in eq 3.7 vs the angle θ for various fixed ϵ_p/ϵ_n values denoted in the figure. For the particle in Figure 2, we have $\epsilon_p/\epsilon_n = 1.95$; the contact angle is $\theta = 114.9°$; the corresponding value of μ is 0.690. The curves in the figure can be reproduced using eq A2 and Table 5.

K. Marinova and Mrs. S. Tcholakova for consulting the experiments, and Ms. M. Paraskova for assistance in the figure preparation.

Appendix: Computation of the Functions $f(\alpha, \epsilon_p/\epsilon_n)$ and $\mu(\theta, \epsilon_p/\epsilon_n)$

To calculate $F^{(n)}$ and p_{el} by means of eqs 3.4 and 3.7, one needs to know the values of the dimensionless quantities $f(\alpha, \epsilon_p/\epsilon_n)$ and $\mu(\theta, \epsilon_p/\epsilon_n)$. The latter two functions are universal in the sense that they are independent of the particle radius, R, and of the surface electric charges and potentials. We computed f and μ by solving numerically the electrostatic boundary problem, as described in sections 5 and 6. The obtained $f(\alpha)$ and $\mu(\theta)$ curves are plotted, respectively, in Figures 4 and 9 for seven different values of the ratio ϵ_p/ϵ_n. Furthermore, we fitted the curves in Figures 4 and 9 by simple polynomial regressions, whose coefficients are given in Tables 4 and 5, respectively. The data in these tables enable one to reproduce relatively easily all curves in Figures 4 and 9, in both numerical and graphic form. Next, by interpolation, one can determine f and/or μ for a given couple of values, $(\alpha, \epsilon_p/\epsilon_n)$ or $(\theta, \epsilon_p/\epsilon_n)$.

We interpolated the computed $f(\alpha)$ curves in Figure 4 by means of the following regression:

$$\ln(f) = b_0 + b_1 \cos\alpha + b_2 \cos^2\alpha + b_3 \cos^3\alpha \qquad \text{(A1)}$$

where $10° \le \alpha \le 170°$. The computed coefficients $b_0, \ldots, b_3$ are listed in Table 4. For all interpolating fits, the correlation coefficient is at least 0.999.

Table 4. Coefficients in eq A1 Which Allow One to Reproduce the $f(\alpha)$ Curves in Figure 4

ϵ_p/ϵ_n	b_0	b_1	b_2	b_3
0.125	0.3840	0.1281	−0.1309	−0.0515
0.250	0.3302	0.0319	−0.1502	−0.0707
0.500	0.2208	−0.1396	−0.1668	−0.1049
1.000	4.465×10^{-3}	−0.4123	−0.1470	−0.1708
2.000	−0.3936	−0.7697	−0.0240	−0.3155
4.000[a]	−1.0437	−1.1201	0.2672	−0.6198
8.000[a]	−1.9633	−1.3468	0.7172	−1.1275

[a] At this value of ϵ_p/ϵ_n, eq A1 is applicable for $10° \le \alpha \le 160°$.

Table 5. Coefficients in eq A2 Which Allow One to Reproduce the $\mu(\theta)$ Curves in Figure 9

ϵ_p/ϵ_n	c_0	c_1	c_2	c_3
0.125	0.4155	−0.8675	0.5818	−0.2869
0.250	0.4020	−0.8361	0.5507	−0.2711
0.500	0.3790	−0.7825	0.5428	−0.3171
1.000	0.3518	−0.7163	0.4652	−0.2676
2.000	0.3206	−0.6319	0.4022	−0.2757
4.000	0.2968	−0.5713	0.3106	−0.1982
8.000	0.2802	−0.5281	0.2404	−0.1359

The values of μ are obtained from fits of numerical data, like those in Figure 8, by means of eq 3.7. The parameter μ accounts for the electrostatic interactions in the very narrow vicinity of the contact line. Therefore, μ is sensitive to the angle θ subtended by the interfaces at the contact line. For this reason, to compute the basic numerical data (like the points in Figure 8), we ran the computer program by formally setting $\alpha = \theta$ in the boundary conditions; see Figure 7. The obtained $\mu(\theta)$ curves are shown in Figure 9. These curves can be excellently fitted (correlation coefficient better than 0.9999) by means of the following regression:

$$\mu = c_0 + c_1 \cos\theta + c_2 \cos^2\theta + c_3 \cos^3\theta \qquad \text{(A2)}$$

The computed coefficients $c_0, \ldots, c_3$ are listed in Table 5. Equation A2, along with the coefficients in Table 5, is applicable for the calculation of $\mu(\theta, \epsilon_p/\epsilon_n)$ for all values of θ and ϵ_p/ϵ_n, for which $0 < \mu < 1$. We found that, for all other values of θ and ϵ_p/ϵ_n, for which the fit gives either $\mu < 0$ or $\mu > 1$, eq 3.7 does not describe well the exact computed $p_{el}(r)$ curves. Consequently, as seen in Figure 9, eqs 3.7 and A2 can be used for $50° < \theta < 130°$, where $0 < \mu < 1$. Fortunately, the latter interval of θ values covers the practically important range of particle contact angles, which provide the formation of stable Pickering emulsions.[14]

LA0497090